

# Design and Integration of a Novel Spatial Articulated Robotic Tail

Wael Saab, *Student Member, IEEE*, William S. Rone, *Student Member, IEEE*, Anil Kumar, *Student Member, IEEE*, Pinhas Ben-Tzvi, *Senior Member, IEEE*

**Abstract**— In nature, tails are a key feature exhibited by a wide variety of animals to help stabilize, maneuver, manipulate and/or propel. However, previous research into robotic tails has focused on limited-degree-of-freedom (DOF), pendulum-like structures designed to perform a specific task. This paper presents a novel robotic tail design capable of spatial motion to perform several functionalities utilizing a single structure. The roll-revolute-revolute robotic tail (R3-RT) is a multi-link robotic structure with a roll-DOF at the tail base, and two independently actuated co-planar bending segments composed of several links connected by revolute joints. A dynamic model of the tail is presented, along with considerations for sensing the robot's state and controlling the tail. The inertial loading capabilities of the tail are analyzed using the dynamics model, and experiments with an integrated prototype of the R3-RT are performed to validate the dynamic model, inertial loading analysis and benefits of tail articulation. A case study using a virtual quadruped model with the R3-RT is also presented to analyze the impact of the tail loading on yaw-angle maneuvering.

**Index Terms**— Mobile Robots, Robotic Tail, Hyper-redundant Robot, Cable-Driven, Legged Robot

## I. INTRODUCTION

IN nature, tails are used to assist propulsion, stabilization, maneuvering, and manipulation. However, in robotic systems, the dominant paradigm has been to focus on leg design and control to simultaneously achieve propulsion, maneuvering and stability. However, by offsetting some of the required functionality for maneuvering and stabilization to a tail, the leg's design and control complexity could be reduced.

The roll-revolute-revolute robotic tail (R3-RT) is a spatial tail structure capable of improving legged robot maneuverability and stabilization. This paper focuses on the design, modeling and implementation of the R3-RT, with more detailed future work planned for task planning and state-space control. The R3-RT is part of ongoing research studying the design and implementation of articulated robotic tails capable of augmenting a legged robot's ability for agile and robust terrain traversal in unstructured environments [1, 2].

## II. BACKGROUND AND DESIGN MOTIVATION

### A. Inertial Adjustment Mechanisms – Prior Work

This section reviews inertial adjustment mechanisms that can generate loading at their attachment point independent of

ground contact. These mechanisms can be classified as: 1) substrate interaction mechanisms, such as propellers or thrusters that propel the surrounding environment to produce force, 2) translational mechanisms, such as a reaction mass, that can generate reaction forces and adjust center of mass (COM) location [3], and 3) rotational mechanisms, include symmetric systems such as reaction wheels that have the COM constrained along the axis of rotation and can provide reactive moments, and asymmetrical systems such as pendulums and robotic tails that generate reactive forces and moments and adjust the COM location.

Neither substrate interaction nor translational mechanisms are practical onboard a legged robot due to size and weight requirements. However, reaction wheels can fit in small volumes and continuously rotate, but their performance is limited by mass constraints and the actuator angular velocity [4]. A robotic tail requires a larger workspace but can be designed with a much larger moment of inertia due to the length over which mass is distributed. Comparative analysis of the angular impulse between tails and reaction wheels has shown that a tail is more appropriate when space is available for a high moment of inertia mechanism and the time frame of inertial adjustments is relatively short, whereas reaction wheels provide moments over infinite rotational stroke and longer time scales [4]. Thus, tails are best suited for aggressive inertial adjustment applications for mobile robotic systems [5].

### B. Existing Robotic Tail Designs

Many of the robotic tails proposed in literature draw inspiration from animals such as cheetahs [6-8], kangaroos [9], fish [10], and lizards [11]. To facilitate a comparison of prior tails to the R3-RT, a sample of existing robotic tail designs is presented in Table 1. In terms of mechanical design, the majority of research has focused primarily on single-body planar pendulums and covers a wide range of masses (17 to 1000 g) and lengths (73 to 500 mm). Planar tails operate along a single-DOF either in the pitch- [7, 11, 12], yaw- [10, 13-15] or roll-direction [8]. Spatial tails are constructed from two-DOF, single-mass pendulums that operate in a combination of planes, such as pitch-yaw [6, 16-19]. Planar tails provide enhanced performance about a single body-axis with the advantage of simple design and control. Spatial tails greatly increase workspace and provide multi-axis performance at the cost of increased design and control complexity.

Functionally, these tails may be classified as aiding propulsion, stabilization or maneuvering. Tails for propulsion include fish-like swimming [10], assisting acceleration and deceleration [7], and vertical climbing [14]. Tails for stabilization include COM adjustments that aid passive

Date Submitted: October 1, 2017. This material is based upon work supported by the National Science Foundation under Grant No. 1557312.

The authors are with Virginia Tech, Blacksburg VA 24060 USA (email: {waelaab/wsrone/anilks/bentzvi}@vt.edu).

TABLE 1. COMPARISON OF ROBOTIC TAIL DESIGNS, ACTUATION PROPERTIES AND ESTIMATED PEAK MOMENTS PROVIDED AT TAIL BASE.

System	[15]	[7],[8]	[9]	[12] <sup>A</sup>	[11]	[13]	[17]	[6]	[18]	R3-RT
Tail Mass (g)	700	400	371	1000	17	4	70	400	150	900
Tail Length (mm)	150	500	177	500	103	115	73	500	300	500
Rated Motor Power (W)	5.5	120	19 <sup>B</sup>	-	4	2.5 <sup>B</sup>	1.75 <sup>B</sup>	70 ea.	426 <sup>B</sup>	100 ea.
Max. Speed (RPM)	6	275	240 <sup>B</sup>	21	3000	400 <sup>B</sup>	320 <sup>B</sup>	137	353 <sup>B</sup>	260
End-Effector Workspace (Deg)	180	224	220	-	255	265	135/135	180/70	180/180	270/ $\infty$
Mechanical Design	Planar						Spatial			
	Single-Body Rigid Pendulum									Articulated

<sup>A</sup>: Simulation, <sup>B</sup>: Values from [28].

walking [15] and maintain a constant body attitude [16], and dynamic motions for disturbance rejection [19] and airborne attitude control [6, 9, 11, 12, 18]. Tails for maneuvering enable yaw-angle [13] and roll-angle turning [8].

Recent research has analyzed the impact of robotic tail structures, ranging from single body one-DOF pendulums to a six-DOF articulated tail, on the yaw-angle maneuvering of a legged robot [1]. Simulation results indicate that tail articulation can enhance the inertial loading used to yaw-angle maneuver, compared to a pendulum-like tail undergoing a similar motion. Furthermore, multi-segment tails are capable of forming multiple mode shapes that enable greater control over COM positioning (discussed in section VI-A) and generating inertial loading [20]. However, practical implementation of additional articulation requires more complicated mechanical designs and additional actuators for controlled motion. To address these challenges, prior research in high-DOF articulated structures will be considered.

### C. Existing Articulated Robotic Structures

This section reviews previous articulated robots to identify design challenges and highlight useful design criteria that have inspired the R3-RT design. The two main classes of high-DOF articulated robots are continuum and serpentine.

Continuum robots continuously bend along their length. Externally actuated continuum robots have an actuation unit at the base, an actuation transmission system (typically cables or rods), and a structure composed of an elastic backbone that bends along its length. Intrinsically actuated designs integrate actuation along the robot and generate motion from the expansion and contraction of parallel structures. Although continuum robots are capable of forming articulated spatial curvatures, there remain significant challenges in terms of modeling these structures, sensing their state, and performing real-time control due to the absence of conventional joints, all of which are active research topics [21, 22].

Serpentine robots are composed of a serial chain of numerous rigid links and form discrete curvatures. Traditional serpentine robots are actuated at each joint. However, individual joint actuation increases the robot's mass, cross-section, and actuator torque requirements. Another approach separates the robot's structure and actuation using a cable transmission system, similar to extrinsically actuated continuum robots. In these designs, elastic components were utilized to regulate joint rotation [23]. However, this approach requires individual cable actuation since cable displacements are not typically equal during motions. Alternatively, rolling contact joints with specially designed contours have been proposed to maintain equal antagonistic cable displacements

and overcome the elastic elements' joint angle limits. These two active cables may be connected to a single driving pulley, which reduces the number of actuators [24]. Decoupling multi-segment curvature actuation utilizing a hollow backbone for neutral axis cable routing has been proposed by [23].

The merits of extrinsic actuation in serpentine robots have been widely demonstrated in robotic hand/finger and gripper designs that commonly have more joints than actuators to reduce manipulator size and inertia. Fixed motion coupling can distribute angles via gear trains [25], closed belts/pulleys [26], and linkages [27] that provide structural rigidity and accurate trajectory tracking. Cable transmission systems have also been used to produce motion in combination with angle distribution methods such as friction pulleys [28], higher order rolling pairs [29], and spring-loaded joints [30].

### D. Design Motivation and Requirements

Three requirements driving the tail's design have been formulated. First, the tail should be spatial and significantly multi-functional, capable of affecting the mobile robot both dynamically and quasi-statically. Quasi-static loading reconfigures the tail to modify the system's COM position. Therefore, the tail should have a large workspace to maximize the system COM adjustments. Dynamic loading utilizes rapid tail motions to generate high-magnitude inertial loading to affect the system dynamics. A spatial tail will enable loading in the yaw, pitch and roll directions. While the tail structure will not be able to apply an arbitrary loading profile with forces decoupled from moments, it should be capable of generating significant moments about all directions.

Second, the mechanism should be articulated and capable of forming multiple curvatures. As discussed in [1, 20], an articulated structure enhances the tail's loading compared to a pendulum-like structure. The authors choose a serpentine articulated structure due the conventional means of design, modeling, and sensing. Extrinsic actuation transmitted by cabling is chosen to reduce the minimum tail size, inertia and actuator loads. A fixed motion coupling constrains tail segments, and cables routed along contoured cylindrical links will be used to decouple the tail segments' actuation while ensuring equal and opposite antagonistic cable displacement.

Third, the tail must be designed to operate in a cantilevered mode. Several macro-scale articulated robots are designed for vertical operation (i.e., [39], [40]) without consideration for cantilevered mounting. The tail design should be capable of remaining fully extended with minimal to no actuation.

### E. Contributions

Based on the design requirements defined in section II-D, a novel spatial tail is proposed that provides the following contributions relative to pendulum-like robotic tails and serpentine robots in literature: (1) Novel implementation of a flexible tail structure capable of forming two mechanically decoupled tail curvatures (mode-shapes), (2) Enhanced COM and end-effector workspaces due to the two independent tail segments (section VI-A), (3) Experimentally-verified enhanced inertial loading capabilities of the articulated tail compared to a pendulum-like tail (section VII-C), and (4) Spatial tail curvatures enabled via an infinite roll rotation that has the capacity of operating as both a symmetrical (about the roll axis) and asymmetrical inertial adjustment mechanism (section VI-B).

## III. MECHANICAL DESIGN

### A. Rigid Housing and Actuation Unit

The R3-RT mechanical design, shown in Fig. 1, consists of a rigid housing, actuation unit and tail segments. The rigid housing consists of two frames connected together with steel rods to provide lightweight, structural support to the R3-RT. Bearings and an internal gear, integrated into the rigid housing, meshes with the actuation unit spur gear (Fig. 2) to enable the roll-DOF rotation; this roll is measured with an absolute encoder mounted to the rear frame and coupled to the actuation unit via a timing belt. A high-current-capacity, miniature slip ring (Orbex 300 Series) transmits control signals and motor current to the actuation unit. The slip ring enables the tail to continuously roll without the risk of breaking wires. This allows the R3-RT to act like a reaction wheel when the tail segments are bent such that the tail segments' COM aligns with the roll axis, in addition to acting as an asymmetrical rotational inertial adjustment mechanism.

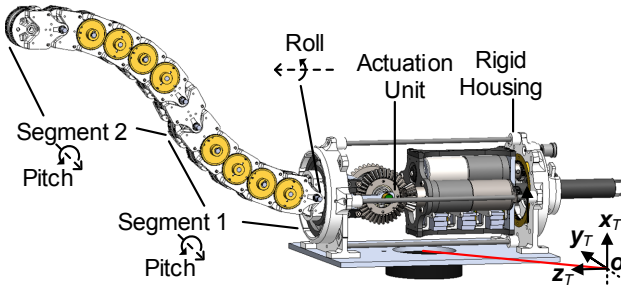


Fig. 1. R3-RT system design.

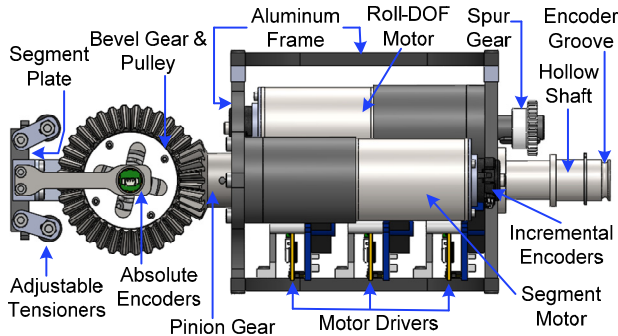


Fig. 2. R3-RT actuation module.

This is a significant advantage over prior tail designs (Table 1) with more constrained workspaces (section VI-A).

The tail actuation unit (Fig. 2) consists of three gear motors: one for the roll-DOF, and two for the tail segment DOFs. The roll-DOF motor is attached to a spur gear that meshes with an internal gear located in the rigid housing. Each segment gear motor is coupled to a two-channel pulley (not visible in Fig. 2, located behind the bevel gear) through a pinion/bevel gear reduction. The pulleys are rigidly connected to the bevel gear and the antagonistic cable pair used to actuate the motor's tail segment. Four adjustable tensioning mechanisms with passive rollers provide a means of individually tensioning each of the four cables (two antagonistic cables per actuated segment) to ensure a straight home configuration and minimize backlash.

### B. Tail Segments

Figure 1 shows the overall tail design concept. Twelve bodies (links 1-12) are connected serially to create a two-segment robotic tail capable of “bending” in the pitch direction. Link 1 is connected to link 0 through a pitch-direction revolute joint (when the roll angle is zero as depicted in Fig. 1), which is rigidly attached to the actuation unit's segment plate (Fig. 2).

The remaining 11 links are connected by revolute joints parallel to the joint between links 0 and 1. As a consequence of this design, when the roll angle is  $\pm 90^\circ$ , the tail remains extended without requiring cable actuation (per the cantilevered-operation design requirement in section II-C). Distinct segments are created by terminating pairs of antagonistic cables along the robot—in Fig. 1, two segments are created by terminating cable pairs at links 6 and 12.

The R3-RT decouples multi-curvature actuation and ensures equal antagonistic cable displacements through its link design and cable routing scheme. Cables are routed along nested cylindrical surfaces built into the links to ensure equal cable extension/retraction of the antagonistic cable pair during tail motion. Figure 3(a) illustrates this configuration and shows cable routing for a four-link segment that resembles the cable routing scheme to actuate segment 1 (where two cables are terminated at the end link within the tail segment and the left link is considered fixed ground). The antagonistic cable displacements are defined by the linear relationship  $\pm r_{cbl}\theta_i$ , where  $r_{cbl}$  is the radius of the cylindrical contour and  $\theta_i$  is the relative link rotation. The nested cylinder cable routing

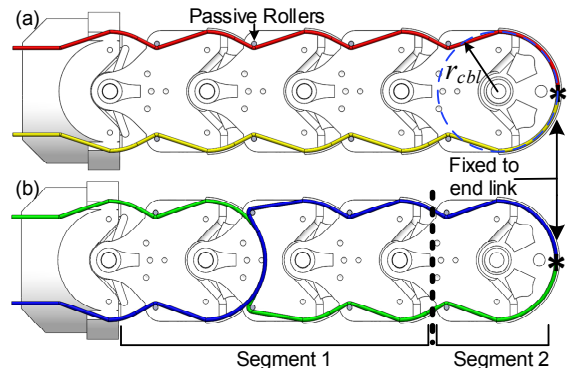


Fig. 3. R3-RT cabling concepts: (a) segment bending arrangement, (b) S-path arrangement.

approach enables the use of a single pulley to control the extension and retraction of an antagonistic cable pair without the need to account for variance in cable extension and retraction. This is because the joint angles increase and decrease the cable path by equal angles on each side over the same radius.

To simplify control, the actuation of segments 1 and 2 are mechanically decoupled. Two cables terminate at link 12 in segment 2 and rout through this segment similar to segment 1 shown in Fig. 3(a). However, in segment 1, the segment 2 cabling routes along an S-path and crisscrosses in the middle of segment 1 as shown in Fig. 3(b). With this S-path routing, the first and second halves of the cable path will extend and shorten the cable path by equal amounts, or vice versa (the first and second halves will shorten and extend). This routing creates a null space for the segment 2 actuation cabling with respect to the motion of segment 1. However, this assumes that the joint angles along the segment are all equal.

To ensure the 6 joint angles are equal within a segment, the R3-RT utilizes 5 gear pairs mounted along the segment. The gears in each pair are mounted on two links with a single link separating them, as shown in Fig. 4(a). For example, in gear pair 1, the first gear (red) meshes with the second gear (purple) with an intermediate link (yellow) separating the gears' associated rigid bodies.

To ensure equal angles along the segment, the gears in each pair have equal pitch diameters. For the gear pair associated with three sequential links  $i-1$ ,  $i$  and  $i+1$ , shown in Fig. 4(b), gears are rigidly attached to links  $i-1$  and  $i+1$ , with link  $i$  separating the links. If link  $i-1$  is held fixed, link  $i$  will rotate by angle  $\theta$  relative to link  $i-1$ , and link  $i+1$  will rotate by  $\theta$  relative to link  $i$ . This is done for the five sequential triplets of links 0-6 (segment 1) and 6-12 (segment 2).

#### IV. SENSING, ACTUATION AND ELECTRICAL DESIGN

##### A. Sensing

Two types of joint-space sensing are integrated into the R3-RT's actuation module: angular position (roll or cable pulleys) and motor rotor speed. The three position measurements are generated by absolute encoders (US Digital MA3) coupled to the hollow shaft (roll DOF, Fig 2) or cable pulleys (segment

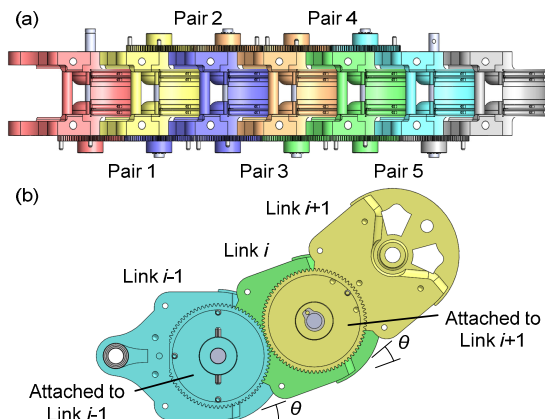


Fig. 4. R3-RT gearing: (a) single-segment gear arrangement, (b) angle constraint from gear pair. Parts sharing a color are rigidly attached.

DOFs). The roll-DOF encoder fits into the rear frame of the rigid housing and is coupled to the actuation module using a timing belt mounted to the groove shown in Fig. 2. The two segment-DOF encoders are shown coupled to the cable pulley in Fig. 2 through the bevel gear. Motor rotor angular velocity for each motor is estimated by an incremental encoder (US Digital E4T) mounted to the motor.

##### B. Actuation

To generate high inertial loading, the R3-RT is actuated using three Maxon 100 W brushless DC motors (ECi 40) in closed-loop position control. These motors were chosen to exceed the torque requirements for experiments presented in this analysis to provide an experimental test platform capable of analyzing a wide variety of potential tail structures with various dimensions and mass properties. Gear reductions were selected to balance considerations for cable speed and force requirements estimated for a range of possible robotic tails.

As discussed in section III-C, two of the three motors control the independent bending of the R3-RT segments through antagonistically-actuated cable mechanisms. A bevel gear train with 2:1 reduction drives the cable pulley, and a gearbox with reduction 51:1 drives the pinion gear. The pulley radius matches the cylindrical cable routing radius  $r_{cbl}$  of the linkages, which makes the pulley rotation and segment bending angle equal (e.g., if the segment 1 pulley rotates  $45^\circ$ , segment 1 will bend  $45^\circ$ ).

The third motor controls the R3-RT actuation module roll-angle using a spur gear coupled to an internal gear (with a gear reduction of 3:1 in addition to a 51:1 gearbox). Incorporating the roll motor within the actuation unit reduces the rigid housing cross-section at the cost of increased power required to produce roll motion due to the additional inertia. However, in this design, the motors are close to the roll axis, minimizing their contributions to the net actuation unit inertia.

##### C. Electrical Design

Figure 5 shows the R3-RT's electrical design. To control the system, two Teensy 3.2 ARM microcontrollers (MCUs) are used, with one acting as master and the other as slave. These MCUs communicate over an UART link through the slip ring. The master MCU is mounted to the rigid housing and connects the user PC and the slave MCU. The master

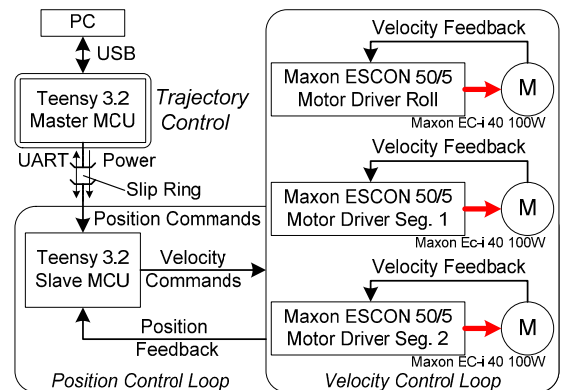


Fig. 5. R3-RT electrical design with inner-loop velocity control and outer-loop position control. M denotes motor.

MCU receives the three desired joint angle trajectories from the user, interpolates this data into position set points and sends these set points to the slave MCU. The master MCU also allows the user to exercise software control over motor power through a high side MOSFET switch. The master MCU housing also connects the power supply to the slip ring through an emergency cut-off switch.

The slave MCU is incorporated into the actuation module to ensure stable connections with the sensors and motor drivers. The slave MCU is programmed as a PD controller to control the three motors in closed-loop position control mode. The slave MCU obtains the three angles from the absolute encoders and sends speed commands to the motor drivers, with proportional gain of  $230 \text{ s}^{-1}$  and differential gain of 28.6. The controller gain coefficients were tuned for near-critical operation on the bases of empirical analysis. The position control loop operated at a control frequency of 450 Hz that is sufficient to track fast tail trajectories accurately (section VII).

Each motor is controlled by a motor driver (Maxon ESCON 50/5) operating a PI velocity control loop. These motor drivers receive velocity commands from the slave MCU and regulate current to the motors using a proportional gain of 450 N-m/s/rad and an integral gain of 2.0 N-m/rad.

## V. TAIL MODELING

### A. Model Overview

The tail model has three inputs—two prescribed cable displacements  $\delta_k$  and a prescribed tail roll rotation  $\varphi$ —and five outputs—two segment joint angles  $\beta_k$  (each joint angle in a given segment is equal), two cable tensions  $T_k$  and a roll-DOF torque  $\tau$ . Internal state variables include the five outputs, along with 10 gear forces  $F_{k,j,gear}$  between the segment  $k$  gear pair  $j$ .

The 13 revolute joints lead to 13 equations of motion. If the net moment  $\mathbf{M}_{i,jnt}$  is calculated at joint  $i$ , the dot product of  $\mathbf{M}_{i,jnt}$  and the joint  $i$  axis unit vector  $\boldsymbol{\varsigma}_i$  equals zero, as a revolute joint cannot support a moment about its joint axis. This is defined in Eq. 1, where  $\mathbf{R}_i$  is the link  $i$  orientation matrix, and  $\mathbf{y}$  and  $\mathbf{z}$  are the  $y$ - and  $z$ -axis unit vectors. Four loading effects contribute to  $\mathbf{M}_{i,jnt}$ : gravity ( $\mathbf{M}_{i,grv}$ ), inertia ( $\mathbf{M}_{i,inr}$ ), gearing ( $\mathbf{M}_{i,gear}$ ), and actuation ( $\mathbf{M}_{i,act}$ ), shown in Eq. 2.

$$\boldsymbol{\varsigma}_i \cdot \mathbf{M}_{i,jnt} = 0, \quad \boldsymbol{\varsigma}_i = \begin{cases} \mathbf{R}_i \mathbf{z}, & i = 0 \\ \mathbf{R}_i \mathbf{y}, & i > 1 \end{cases} \quad (1)$$

$$\mathbf{M}_{i,jnt} = \mathbf{M}_{i,inr} - \mathbf{M}_{i,grv} - \mathbf{M}_{i,gear} - \mathbf{M}_{i,act} \quad (2)$$

In addition, the model in this section is defined with respect to the tail frame  $ox_T y_T z_T$  (frame T) at the tail base. This frame is considered to be stationary in sections V-VII. Section VIII will consider the motion of this frame attached to a quad.

### B. Kinematic Model

First, the tail kinematics are defined. Due to system geometry, there is a fixed relationship between  $\delta_k$  and  $\beta_k$ , defined in Eq. 3, where  $r_{cbl}$  is the cable routing cylinder radius (Fig. 6). Using these two segment joint angles, a vector of the pitch joint angles  $\theta_i$  may be defined using Eq. 3. Using  $\varphi$  and  $\theta_i$ ,  $\mathbf{R}_i$  is defined using Eq. 4, where  $\mathbf{R}_z(\varphi)$  and  $\mathbf{R}_y(\theta)$  denote  $z$ - and  $y$ -axis rotations by angles  $\varphi$  and  $\theta$ , respectively.

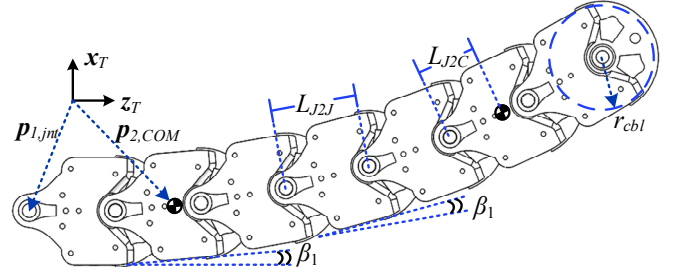


Fig. 6. R3-RT kinematic variables.

$$\beta_k = \delta_k / (6r_{cbl}), \quad \theta_i = \begin{cases} \beta_1, & 1 \leq i \leq 6 \\ \beta_2, & 7 \leq i \leq 12 \end{cases} \quad (3)$$

$$\mathbf{R}_i = \begin{cases} \mathbf{R}_z(\varphi) & i = 0 \\ \mathbf{R}_{i-1} \mathbf{R}_y(\theta_i) & i > 0 \end{cases} \quad (4)$$

Using  $\mathbf{R}_i$ , the joint positions  $\mathbf{p}_{i,jnt}$  and link COM positions  $\mathbf{p}_{i,COM}$  may be calculated using Eqs. 5 and 6, where  $\mathbf{p}_{0,jnt,lcl}$  is the position from the frame T origin to joint 0,  $\mathbf{p}_{1,jnt,lcl}$  is the position from joint 0 to joint 1,  $L_{J2J}$  is the distance between two adjacent pitch joints,  $\mathbf{p}_{0,COM,lcl}$  is the position from joint 1 to the link 0 COM and  $L_{J2C}$  is the distance between a pitch joint and its COM. In addition,  $\mathbf{p}_{i,j,J2C}$  in Eq. 7 defines the positions from joint  $i$  to the link  $j$  COM.

$$\mathbf{p}_{i,jnt} = \begin{cases} \mathbf{p}_{0,jnt,lcl} & i = 0 \\ \mathbf{p}_{i-1,jnt} + \mathbf{R}_{i-1} \mathbf{p}_{1,jnt,lcl} & i = 1 \\ \mathbf{p}_{i-1,jnt} + L_{J2J} \mathbf{R}_{i-1} \mathbf{z} & i > 1 \end{cases} \quad (5)$$

$$\mathbf{p}_{i,COM} = \begin{cases} \mathbf{p}_{i,jnt} + \mathbf{R}_i \mathbf{p}_{0,COM,lcl} & i = 0 \\ \mathbf{p}_{i,jnt} + L_{J2C} \mathbf{R}_i \mathbf{z} & i > 0 \end{cases} \quad (6)$$

$$\mathbf{p}_{i,j,J2C} = \mathbf{p}_{j,COM} - \mathbf{p}_{i,jnt} \quad (7)$$

For rotational kinematics, the link  $i$  angular velocities  $\boldsymbol{\omega}_i$  are defined in Eq. 8 for the roll ( $i = 0$ ) and pitch ( $i > 0$ ) joints, where  $\dot{\varphi}$  denotes the first time derivative of  $\varphi$ .

$$\boldsymbol{\omega}_i = \begin{cases} \dot{\varphi} \mathbf{z} & i = 0 \\ \boldsymbol{\omega}_{i-1} + \dot{\theta}_i \mathbf{R}_{i-1} \mathbf{y} & i > 0 \end{cases} \quad (8)$$

### C. Dynamic Model

The gravitational moment  $\mathbf{M}_{i,grv}$  at joint  $i$  is due to the gravitational forces  $\mathbf{F}_{j,grv}$  acting on links  $i$  through 12. Equation 9 defines  $\mathbf{M}_{i,grv}$  and  $\mathbf{F}_{j,grv}$ , where  $m_{j,L}$  is the link  $j$  mass,  $g$  is gravitational acceleration,  $\boldsymbol{\zeta}_{grv} = -\mathbf{x}_T$  is the gravity direction unit vector and  $\tilde{\mathbf{a}} \mathbf{b}$  denotes  $\mathbf{a} \times \mathbf{b}$ .

$$\mathbf{M}_{i,grv} = \sum_{j=i}^{12} \tilde{\mathbf{p}}_{i,j,J2C} \mathbf{F}_{j,grv}, \quad \mathbf{F}_{j,grv} = m_{j,L} g \boldsymbol{\zeta}_{grv} \quad (9)$$

Similar to  $\mathbf{M}_{i,grv}$ , the inertial moment  $\mathbf{M}_{i,inr}$  depends on the links ‘downstream’ of the joint. For joint  $i$ , Eq. 10 defines the inertial moment generated by links  $i$  through 12, where  $\mathbf{I}_{j,L,lcl}$  is the link’s local moment of inertia,  $\dot{\boldsymbol{\omega}}_j$  is the body  $j$  angular acceleration and  $\ddot{\mathbf{p}}_{j,COM}$  is the body  $j$  COM acceleration.

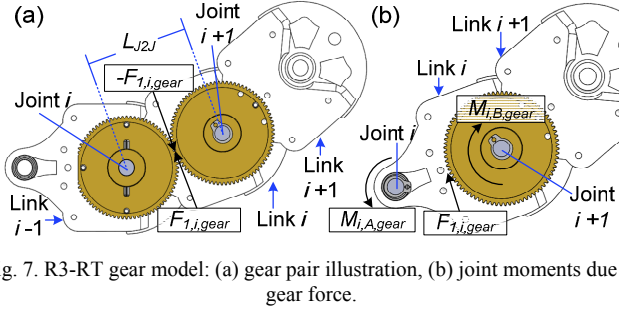


Fig. 7. R3-RT gear model: (a) gear pair illustration, (b) joint moments due to gear force.

$$\mathbf{M}_{i,inr} = \sum_{j=1}^{12} (\mathbf{M}_{j,inr,b} + \tilde{\mathbf{p}}_{i,j,J2C} \mathbf{F}_{j,inr,b}), \quad \mathbf{I}_{j,L} = \mathbf{R}_j \mathbf{I}_{j,L,lcl} \mathbf{R}_j^T, \quad (10)$$

$$\mathbf{M}_{j,inr,b} = \mathbf{I}_{j,L} \dot{\boldsymbol{\omega}}_j + \tilde{\boldsymbol{\omega}}_j \mathbf{I}_{j,L} \boldsymbol{\omega}_j, \quad \mathbf{F}_{j,inr,b} = m_{j,L} \ddot{\mathbf{p}}_{j,COM}$$

The gear loading associated with each gear pair will affect the two joints separating that gear pair. Fig. 7 shows that the force applied on link  $i+1$  will contribute to the gear moment at joints  $i$  and  $i+1$ . The impact of force  $F_{k,j,gear}$  (from  $j$ th gear pair in segment  $k$ ) may be mapped into two terms— $M_{i,A,gear}$  and  $M_{i,B,gear}$ —defined in Eqs. 11 and 12. The  $A$ -term accounts for the link  $i+1$  gear force acting on joint  $i$ , and the  $B$ -term accounts for the link  $i+1$  gear force acting on joint  $i+1$ , with the assumption that the gear force acts tangentially to the gear's pitch diameters. For each joint, Eq. 13 defines  $\mathbf{M}_{i,gear}$ .

$$\mathbf{M}_{i,A,gear} = \begin{cases} 0 & i = \{0, 6, 12\} \\ 0.5L_{J2J}F_{1,i,gear} & i = \{1, \dots, 5\} \\ 0.5L_{J2J}F_{2,i-6,gear} & i = \{7, \dots, 11\} \end{cases} \quad (11)$$

$$\mathbf{M}_{i,B,gear} = \begin{cases} 0 & i = \{0, 1, 7\} \\ -0.5L_{J2J}F_{1,i-1,gear} & i = \{2, \dots, 6\} \\ -0.5L_{J2J}F_{2,i-7,gear} & i = \{8, \dots, 12\} \end{cases} \quad (12)$$

$$\mathbf{M}_{i,gear} = (\mathbf{M}_{i,A,gear} + \mathbf{M}_{i,B,gear}) \boldsymbol{\varsigma}_i \quad (13)$$

The actuation moment  $\mathbf{M}_{i,act}$  takes different forms depending on the joint, as shown in Eq. 14. For joint 0, the roll-torque acts directly on the joint, but for joints 1 through  $n$ , the actuation cabling generates a moment in the joint.

$$\mathbf{M}_{i,act} = \begin{cases} \tau \boldsymbol{\varsigma}_i & i = 0 \\ (T_1 + T_2) r_{cbl} \boldsymbol{\varsigma}_i & 1 \leq i \leq 3 \\ (T_1 - T_2) r_{cbl} \boldsymbol{\varsigma}_i & 4 \leq i \leq 6 \\ T_2 r_{cbl} \boldsymbol{\varsigma}_i & 7 \leq i \leq 12 \end{cases} \quad (14)$$

For each antagonistic cable pair, a single real-valued

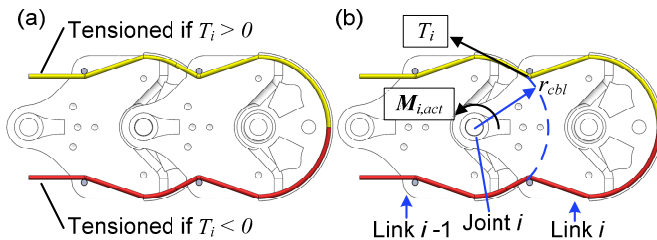


Fig. 8. R3-RT cable model: (a) single-variable tension representation, (b) joint moment due to cable tension.

variable  $T_k$  will represent the non-zero tension in each cable pair. Because cabling cannot carry a negative tension, the symmetric antagonistic loading allows for equal and opposite bi-directional tensioning—the “upper” cable is in tension when  $T_k > 0$ , and the “lower” cable is in tension when  $T_k < 0$ , as shown in Fig. 8(a). The mapping of the cable tension into a joint moment is illustrated in Fig. 8(b)—the cable tension vector aligns with the actuation cabling between links  $i-1$  and  $i$  and the distance is assumed to be  $r_{cbl}$ . In Eq. 14, the difference in  $\mathbf{M}_{i,act}$  definitions for joints 1-3 and 4-6 is due to the S-path routing: as the segment 2 cabling routes through segment 1, its impact on joints 1-3 and 4-6 will be equal and opposite.

Using this model, the solutions for  $\tau$ ,  $T_k$  and  $F_{k,j,gear}$  (the model's internal state variables) may be found in three steps: 1) calculating  $T_2$  and  $F_{2,j,gear}$  for segment 2, 2) calculating  $T_1$  and  $F_{1,j,gear}$  for segment 1 using  $T_2$ , and 3) calculating  $\tau$ .

## VI. TAIL ANALYSIS

### A. Work Space Analysis

The proposed articulated mechanism can form multi-curvature spatial tail configurations for enhanced flexibility and increased workspace. Figure 9 shows the R3-RT's two mode shapes: mode shape 1 is a C-shape with segments bent in the same direction, and mode shape 2 is an S-shape with the segments bent in opposite directions.

The end effector and COM workspaces are defined by the loci of positions the end effector tip (link 12) and COM can reach, respectively. The end effector workspace can be computed using the forward kinematics (section V-B) based on the geometric parameters extracted from the R3-RT CAD and prototype (Figs. 1 and 12), defined in Table 2. Figure 9 shows the R3-RT's simulated planar workspaces (end effector and COM) with roll fixed at  $90^\circ$ . The workspaces have been generated using  $300 \times 300$  input combinations of the pulley angle inputs (resolution:  $0.6^\circ$  and  $0.9^\circ$  for spool ranges  $\pm 90^\circ$  and  $\pm 135^\circ$ , respectively). The coordinate frame origin is the R3-RT joint 1. The  $\pm 135^\circ$  spool rotation range is associated with the maximum R3-RT workspace possible without link 12 interfering with the rigid housing.

A tail's COM workspace is defined by its range of motion, mass distribution, link geometry, and number of independently

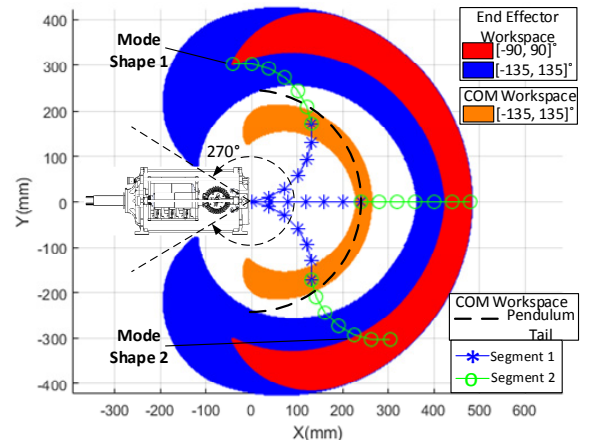


Fig. 9. Workspace and mode shapes of a 12 link, 2 segment R3-RT.

actuated tail segments. For the R3-RT, the COM workspace, with no added tip-mass, is simply the end effector workspace scaled down, as shown in Fig. 9. In a single plane, the R3-RT has a COM workspace that spans  $190^\circ$ . The reported workspace criteria presented in Table 1 for existing pendulum-like tails represents both the end effector and COM workspace since the mass is connected to the tip of a pendulum-like structure. However, for planar pendulum-like tails, the locus of points along which its COM can be moved is constrained along a circular arc (illustrated in Fig. 9); if a spatial pendulum is considered, this arc becomes a spherical surface. Compared to this, the R3-RT produces a higher dimensionality end-effector workspace due to its increased articulation and has significantly greater ability to adjust its COM due to the ability to change the distance between the COM and tail base. However, the R3-RT COM workspace shown in Fig. 9 falls  $65^\circ$  short of [11], but this deficit can be overcome by adding a 450 g tip mass to match the  $255^\circ$  COM workspace and further increase the COM workspace volume.

TABLE 2. R3-RT SIMULATION PROPERTIES.

$r_{cbl}$	25 mm	$L_{J2J}$	40 mm	$L_{J2C}$	32.7 mm
$m_{0,L}$	3.144 kg	$m_{\{1-12\},L}$	0.0759 kg	$p_{0,jm,lcl}$	92.1x mm
$p_{1,int,lcl}$	159.24z mm	$p_{0,COM,lcl}$	$[-3.52, 0, -7.33]^T$ mm		
$I_{0,B,lcl,xx}$	0.01197 kg-m <sup>2</sup>	$I_{0,B,lcl,yy}$	0.01205 kg-m <sup>2</sup>	$I_{0,B,lcl,zz}$	0.004202 kg-m <sup>2</sup>
$I_{\{1-12\},B,lcl,xx}$	0.0001868 kg-m <sup>2</sup>	$I_{\{1-12\},B,lcl,yy}$	0.0000813 kg-m <sup>2</sup>	$I_{\{1-12\},B,lcl,zz}$	0.0001626 kg-m <sup>2</sup>

### B. Tail Base Loading

When the tail is mounted to a load cell or mobile robot, an internal force  $\mathbf{F}_B$  and moment  $\mathbf{M}_B$  acting on the rigid housing is generated, along with equal and opposite loading  $\mathbf{F}_T$  and  $\mathbf{M}_T$  acting on the load cell or robot. The loading  $\mathbf{F}_B$  and  $\mathbf{M}_B$  depends on the inertia of the tail's moving links and the gravitational forces acting at the tail's moving COM. All of these calculations are performed with respect to frame  $ox_Ty_Tz_T$  (considerations for the motion of this frame will be discussed in section VIII-A). As the gear and actuation loading are internal loading effects, they do not contribute to  $\mathbf{F}_B$  or  $\mathbf{M}_B$ .

Equations 15 and 16 define  $\mathbf{F}_B$  and  $\mathbf{M}_B$ , where  $m_F$  is the mass of the rigid housing,  $\mathbf{F}_{F,grv}$  is the rigid housing's gravitational loading and  $\mathbf{p}_{F,COM}$  is the position of the rigid housing COM relative to the base frame.

$$\mathbf{F}_B = -\mathbf{F}_{F,grv} + \sum_{i=0}^n (\mathbf{F}_{i,inv} - \mathbf{F}_{i,grv}), \quad \mathbf{F}_{F,grv} = m_F \mathbf{g} \zeta_{grv} \quad (15)$$

$$\mathbf{M}_B = -\tilde{\mathbf{p}}_{F,COM} \mathbf{F}_{F,grv} + \sum_{i=0}^n (\mathbf{M}_{i,inv} + \tilde{\mathbf{p}}_{i,COM} (\mathbf{F}_{i,inv} - \mathbf{F}_{i,grv})) \quad (16)$$

### C. Tail Loading Profiles

In order to utilize the R3-RT's kinematic and dynamic models to simulate the tail base loading, the parameters used to calculate  $\mathbf{F}_B$  and  $\mathbf{M}_B$  in Eqs. 15 and 16 are provided in Table 2. These properties match the prototype in section VII, to allow comparison of the simulated and measured results.

In addition, trajectories of  $\delta_k$  and  $\varphi$  are required. For  $\delta_k$ , trajectories of the segment bending angles  $\psi_k$  are defined using a sixth-order polynomial and mapped into  $\delta_k$  (Eq. 17), where  $t$  is the simulation time,  $t_0$  and  $t_f$  are the trajectory start and end times,  $\psi_0$  and  $\psi_f$  are the segment angle start and end values and  $a_{k,i}$  is the  $i$ th order term coefficient for segment  $k$ . The

coefficients are found using the Eq. 18 boundary conditions. A similar process is used to define the roll angle, with  $\varphi$ ,  $\varphi_0$  and  $\varphi_f$  replacing  $\psi_k$ ,  $\psi_0$  and  $\psi_f$ .

$$\psi_k = \begin{cases} \sum_{i=0}^5 a_{k,i} t^i, & t_0 \leq t \leq t_f \\ \psi_f & t > t_f \end{cases} \quad \delta_k = r_{cbl} \psi_k \quad (17)$$

$$\begin{aligned} \psi_k(t_0) &= \psi_0 & \dot{\psi}_k(t_0) &= 0 & \ddot{\psi}_k(t_0) &= 0 \\ \psi_k(t_f) &= \psi_f & \dot{\psi}_k(t_f) &= 0 & \ddot{\psi}_k(t_f) &= 0 \end{aligned} \quad (18)$$

Two case studies are considered: dynamic tail bending for a set of fixed roll angles, and dynamic tail roll for a set of fixed bending angles. For both case studies, the tail's static loading when  $\varphi = \psi_k = 0$  is subtracted from the calculated loading profile trajectories to show the loading as it would impact the legged robot on which the tail is mounted.

Figure 10 illustrates the  $\mathbf{F}_B$  and  $\mathbf{M}_B$  profiles for the first case, where  $(t_0, t_f) = (0, 0.5)$  sec and  $(\psi_0, \psi_f) = (0, 90)^\circ$  with  $\varphi = \{0, 45, 90\}^\circ$ . The z-component of  $\mathbf{F}_B$ , due primarily to centripetal acceleration, is invariant to  $\varphi$ , given that the roll axis is  $z_T$ ; for the  $\mathbf{M}_B$  z-component, as roll increases from  $\varphi = 0$ , the gravitational forces acting over y-axis distances generate a base moment. For the  $\mathbf{F}_B$  x- and y-components, due to the centripetal and tangential accelerations of the tail masses, as  $\varphi$  increases, the time-varying component of  $F_{B,x}$  re-allocates to  $F_{B,y}$ . The moments  $M_{B,x}$  and  $M_{B,y}$  are due to several factors: the moments due to the links' angular acceleration, the moments due to inertial forces from the links' linear acceleration, and the moments due to gravity. Gravity primarily impacts  $M_{B,y}$ —the gravitational moment is greatest when  $\psi = 0$  and least

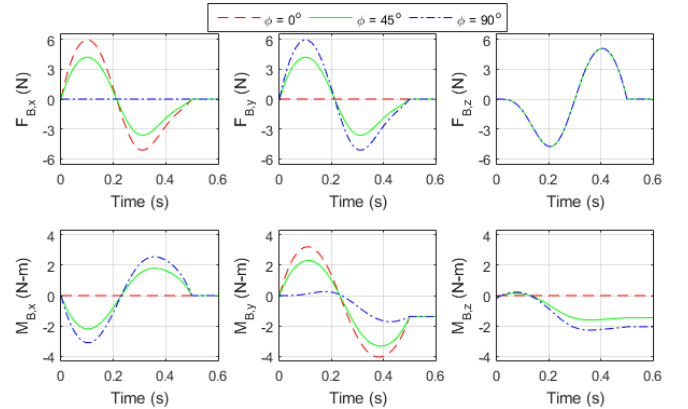


Fig. 10. Simulation Results: Dynamic tail bending loading at fixed roll angles.

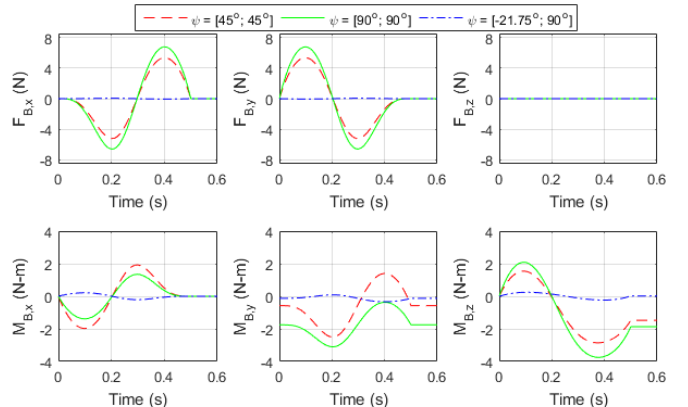


Fig. 11. Simulation Results: Dynamic tail rolling loading at fixed tail bending.

when  $\psi = 90^\circ$ . As with force, the roll angle re-allocates the inertial component between  $M_{B,x}$  and  $M_{B,y}$ .

Figure 11 illustrates the loading profiles for the second case, where  $(t_0, t_f) = (0, 0.5)$  sec and  $(\phi_0, \phi_f) = (0, 90)^\circ$  with  $\psi_1 = \{45, 90, -21.75\}^\circ$  and  $\psi_2 = \{45, 90, 90\}^\circ$ . The set  $\psi = [-21.75; 90]^\circ$  corresponds to a tail configuration with the tail COM located along the roll axis similar to a reaction wheel. For this case, the tail COM does not move during rotation, hence zero force. However, since the tail is not axisymmetric (i.e., there are off-diagonal terms in the tail's inertia tensor), moments are generated in the x-, y- and z-directions.

For the  $\psi = \{45, 90\}^\circ$  cases, the tail COM is held at a fixed distance along the z-axis, which ensures there is no z-direction, and the forces in the x-y plane are due to centripetal and tangential accelerations. However, gravity will generate moments in  $M_{B,y}$  and  $M_{B,z}$ . For  $M_{B,y}$ , the non-zero initial moments are due to the reduced tail COM distance from the tail base for  $\psi_k = \{45, 90\}^\circ$  compared to  $\psi_k = 0^\circ$  (the static loading for  $\phi = \psi_k = 0^\circ$  includes a y-axis moment component). For  $M_{B,z}$ , as  $\phi$  increases from 0 to  $90^\circ$ , the y-axis distance between the COM and tail base increases, creating a gravitational moment. For the inertial components of  $M_{B,x}$  and  $M_{B,y}$ , the magnitude of the inertial component of loading initially increases in magnitude ( $\psi_k = 45^\circ$ ), and then decreases ( $\psi_k = 90^\circ$ ), due to the varying of the z-axis tail COM coordinate and the distance of the tail COM from the z-axis as  $\psi_k$  increases. For the inertial component of  $M_{B,z}$ , the tail's tangential acceleration generates a slight inertial moment that is secondary to the change due to gravity as  $\psi_k$  increases.

The loading profiles of Fig. 11 can act over extended time durations due to infinite roll motion, similar to a reaction wheel, because of the slip ring; this is a performance advantage compared to existing tails reviewed in section II-B.

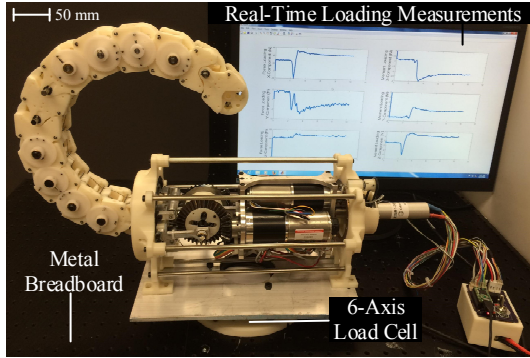


Fig. 12. Experimental set-up of R3-RT.

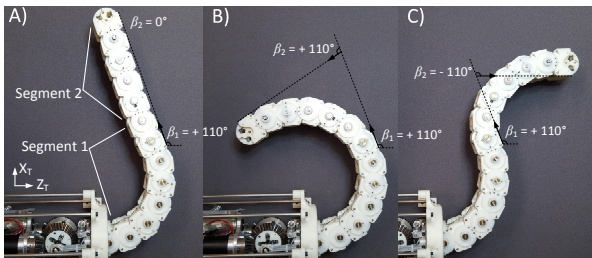


Fig. 13. R3-RT tail decoupled actuation: (a) segment 1 bend while segment 2 remains fixed; (b) mode shape 1, (c) mode shape 2.

## VII. EXPERIMENTAL PROTOTYPE AND MODEL VALIDATION

### A. Tail Implementation

Figure 12 shows the experimental prototype of the R3-RT, and Fig. 13 illustrates the tail's decoupled actuation and mode shapes. The tail's links and rigid housing's frames were printed using ABS plastic. The remaining custom structural components were fabricated from metal (steel for shafts, aluminum for other components). Braided nylon cables (MagicShield) rated for 441 N (100 lbs) were used to actuate the tail; segment 1 actuation required double routed cable lines to accommodate the high impulsive tensions generated during tail motions. During integration, the cable routing was optimized through a series of experimental iterations to minimize friction effects by relieving aggressive cable routing angles about the small sized pins with passive rollers (Fig. 3).

### B. Loading Results

Experiments were performed to measure the tail's ability to generate dynamic loading using a 6-axis load cell as shown in Fig. 12. Sensor measurements were sampled at 400 Hz using a PCI data acquisition card. A moving window mean low-pass filter of width 50 sample points was used to filter out high frequency sensor noise from the measured data; sufficient data was collected preceding the start of the tail motion to uniformly filter the relevant time span.

Tail bending motions, with  $(t_0, t_f) = (0, 0.5)$  sec and  $(\psi_0, \psi_f) = (0, 90)^\circ$  at constant roll angles  $\phi = \{0, 45, 90\}^\circ$ , were performed similar to the case scenarios presented in section VI-C, to compare measured loading profiles with computed simulation results. Figure 14 illustrates the measured loading profiles. Each case scenario was conducted three times with results averaged. From the plot, it can be observed that tail curvature motion is completed in 0.8 sec, after which the tail experiences vibrations that dissipate to steady state conditions.

Compared to simulated results in Fig. 10, the measured loading profiles exhibit similar loading as the roll angle is varied: force loading about the z-axis shows an approximate invariance to various roll angles, gravitational moment loading offsets about the y- and z-axis at final tail configurations approximately match computed results, and profiles qualitatively match the shape of computed profiles and final steady state values, but do not exactly match the idealized smooth contours.

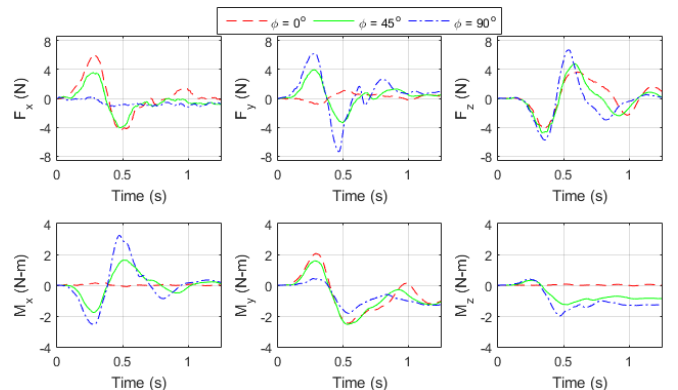


Fig. 14. Experimentally measured loading profiles for fixed-roll experiments.

Measured peak loading profile values, equal to 6 N and 3.1 N-m, fall slightly below computed values because the experimental tail motion duration was slightly longer than the 0.5 s time span used in computed results. This is expected since inertial loading decreases as the time spans of tail motions are lengthened.

### C. Comparing Articulated and Pendulum Inertial Loading

Experiments were performed to compare the inertial loading profiles of an articulated tail structure to a single-body rigid pendulum, a comparison that was analyzed in simulation in [1]. To maintain consistency in terms of mass distribution, the R3-RT tail consisting of 12 links was reconfigured into two structures: 1) an articulated single DOF tail segment with equal relative angle distribution constrained via 11 gear pairs, and 2) a single-body rigid pendulum with immobilized gears capable rotating about its link 1 revolute joint. For consistency in terms of power input and range of motion, both tail structures were actuated by prescribing a constant input cable tension as the tail rotated through its trajectory of equal cable displacement at a fixed roll angle of  $90^\circ$ , thus producing a planar horizontal tail motion unaffected by gravitational loading. The motions result in a COM angular displacement range equivalent to  $104^\circ$  and  $180^\circ$  for the articulated and pendulum-like tail, respectively.

Loading profiles for the articulated and single-body rigid pendulum tails for motions were generated with constant cable tensions of 60 N and 110 N. These motions were performed ten times for each tail structure with measured inertial loading results averaged to ensure consistency. The time spans to complete motions were slower for the articulated tail (60 N: 0.63 s, 110 N: 0.48 s) compared to the pendulum-like tail (60 N: 0.58 s, 110 N: 0.42 s). The articulated tail motions likely require slightly longer time spans due to cable friction along the structure. Table 3 presents the mean measured inertial loading. For equivalent input cable displacements and constant cable tensions, the articulated tail, compared to the pendulum-like tail, on average provides: a 53% increase in generated moment about the base ( $M_{B,X}$ ), a 52% reduction in  $F_{B,Y}$ , and an 8% increase in  $F_{B,Z}$ . Section VIII shows  $M_{B,X}$  contributes 83.9% of the quad’s yaw-angle rotation; therefore, there is significant advantage in increasing its magnitude.

TABLE 3. MEAN MEASURED LOADING PROFILES OF ARTICULATED VS. SINGLE-BODY RIGID PENDULUM TAIL IN CONSTANT TENSION EXPERIMENTS.

Cable Tension	Tail Structure	$F_{B,Z}$ (N)	$F_{B,Y}$ (N)	$M_{B,X}$ (Nm)
60N	Articulated	-2.1	-1.06	-0.48
	Pendulum	-1.89	-2.83	-0.27
110N	Articulated	-6.7	-1.78	-0.93
	Pendulum	-6.36	-3.19	-0.72

These experiments highlight the significance of increased articulation in tail structures to provide enhanced inertial loading about its attachment point in terms of increased moments and reduced forces that produce can produce more desirable effects in applications involving attitude adjustments, dynamic self-righting, and maneuvering as discussed in [19]; results which are corroborated in [1].

### D. Repeatability Results

In addition to analyzing the inertial loading generated by the R3-RT, the accuracy and repeatability of the cable-driven mechanism were also analyzed. This analysis is critical for tasks involving precise COM adjustments, due to the mechanism’s need to effectively transition tension between the pair of cables actuating a segment without impacting the robot’s configuration as it moves through its trajectories.

The R3-RT was programmed to cycle between the tail curvatures C1, C2 and C3 associated with pulley angles of  $0^\circ$ ,  $45^\circ$  and  $90^\circ$  at a fixed roll angle of  $90^\circ$ . To measure the resulting individual joint angles, a Point Grey Blackfly camera (BFLY-U3-13S2M-CS) was mounted orthogonally to the R3-RT’s bending plane. Image processing was used to measure the relative link orientations with respect to the tail’s roll axis using 150 frames for each configuration over five consecutive cycles. Figure 15 shows the expected link angles  $C\#_0$ , and measured link angles  $C\#_m$  for the twelve joints for the three configurations in the form of an error plot showing the measured mean ( $\mu$ ) and standard deviation ( $\sigma$ ).

For the C1 angles, slight offsets are observed from the home configuration—the largest offsets in each segment being  $4.1^\circ$  and  $6.1^\circ$  in segments 1 and 2, respectively. These offsets exist due to discrete meshing of the gear teeth that prevent a perfectly straight home configuration during assembly of the prototype. For configurations C2 and C3, the end links (furthest away from the actuation unit) showed the largest error and repeatability of up to  $10.5^\circ$  and  $\pm 6.7^\circ$ . The primary factors that introduce these inconsistencies are gear backlash and slight cable slack. As each gear pair rotates, slight variations due to the tooth geometry will modify the relative angle between the links. For the cable tensions, a slight slack on one side of the cables is needed to prevent the mechanism from locking up during operation. Lock ups result from highly tensioned segment cables that prevent rotation in either direction and introduce a hysteresis-type effect in the links’ responses to pulley inputs.

## VIII. QUADRUPED MANEUVERING

This section analyzes how the inertial loading generated by the R3-RT can be used to maneuver a quadruped in the yaw-angle direction. This is similar to the analysis in [1], but the foot contact forces, including friction, are neglected.

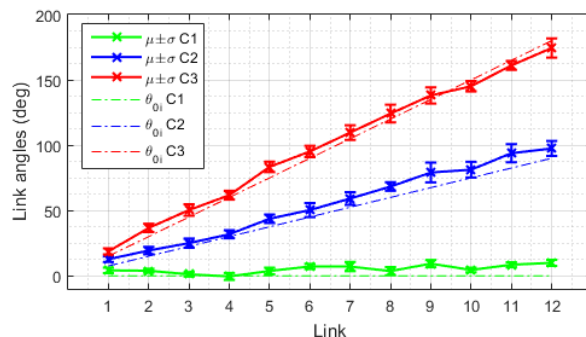


Fig. 15. Repeatability experimental results showing mean and standard deviation of measured link angles and deviations from expected values  $\theta_{0i}$ .

### A. Quad and Tail Model

Figure 16(a) illustrates the concept for the integrated quad and tail structure. The R3-RT is mounted on-board a four-legged robot capable of high-speed running utilizing single-DOF legs currently under development [31]. These legs utilize high-power Maxon brushless DC motors to propel the robot forward, with the tail aiding in stabilization and maneuvering.

To model the yaw-angle dynamic behavior of this system, a kinematic model is needed to connect the quad and tail subsystems. Figure 16(b) illustrates the kinematic variables relative to the quad frame  $ox_Qy_Qz_Q$ , where  $\rho$  is the quad yaw angle,  $\mathbf{p}_T$  is the tail frame position,  $\mathbf{p}_{T,COM}$  is the tail COM position,  $\mathbf{p}_{Q,COM}$  is the quad COM position, and  $\mathbf{p}_{COM}$  is the net system COM position. Both  $\mathbf{p}_T$  and  $\mathbf{p}_{Q,COM}$  are fixed, and  $\mathbf{p}_{T,COM}$  is calculated using Eq. 19, where  $m_F$  is the tail's rigid housing mass,  $\mathbf{p}_{F,COM}$  is the rigid housing COM position relative to the tail frame,  $m_T$  is the total tail mass (Eq. 20) and  $\mathbf{R}_{QT}$  is the orientation of the tail frame relative to the quad frame (Eq. 20). Using  $\mathbf{p}_{T,COM}$ ,  $\mathbf{p}_{COM}$  may be calculated using Eq. 21, where  $m_Q$  is the quad mass, along with  $\mathbf{p}_{C2T}$ , the position vector from the system COM to the tail base frame.

$$\mathbf{p}_{T,COM} = \mathbf{p}_T + \mathbf{R}_{QT} \left( \frac{m_F}{m_T} \mathbf{p}_{F,COM} + \sum_{i=0}^n \frac{m_{i,L}}{m_T} \mathbf{p}_{i,COM} \right) \quad (19)$$

$$\mathbf{R}_{QT} = \mathbf{R}_Y(-90^\circ), \quad m_T = m_F + \sum_{i=0}^n m_{i,L} \quad (20)$$

$$\mathbf{p}_{COM} = (m_Q \mathbf{p}_{Q,COM} + m_T \mathbf{p}_{T,COM}) / (m_Q + m_T) \quad (21)$$

$$\mathbf{p}_{C2T} = \mathbf{p}_{T,COM} - \mathbf{p}_{COM}$$

Equation 22 defines system's planar yaw rotation  $\rho$  dynamics [1], where  $\mathbf{I}$  is the system inertia at its COM (calculated using the parallel axis theorem using the quad mass  $m_Q$  and inertia  $\mathbf{I}_Q$ , fixed link mass  $m_F$  and inertia  $\mathbf{I}_F$  and link mass  $m_{i,L}$  and inertia  $\mathbf{I}_{i,L}$ ),  $\boldsymbol{\omega}$  is the quad angular velocity (Eq. 23), and  $\mathbf{F}_T$  and  $\mathbf{M}_T$  are the tail's loading applied to the quad (Eq. 23). The z-component equation of Eq. 22 is used for the yaw-angle dynamics.

$$\mathbf{I}\dot{\boldsymbol{\omega}} + \tilde{\boldsymbol{\omega}}\mathbf{I}\boldsymbol{\omega} = \mathbf{M}_T + \tilde{\mathbf{p}}_{C2T}\mathbf{F}_T \quad (22)$$

$$\boldsymbol{\omega} = [0 \quad 0 \quad \dot{\rho}]^T, \quad \mathbf{F}_T = -\mathbf{R}_{QT}\mathbf{F}_B, \quad \mathbf{M}_T = -\mathbf{R}_{QT}\mathbf{M}_B \quad (23)$$

Table 4 provides the simulation parameters extracted from the system CAD model shown in Fig. 16(a) used in this analysis, along with the tail properties in section VI. The tail gravity unit vector  $\boldsymbol{\zeta}_{grv}$  for this section is defined in Eq. 24.

$$\boldsymbol{\zeta}_{grv} = -\mathbf{R}_{QT}^T \mathbf{x} \quad (24)$$

### B. Simulation Results

Using this model, the impact of the tail's force and moment

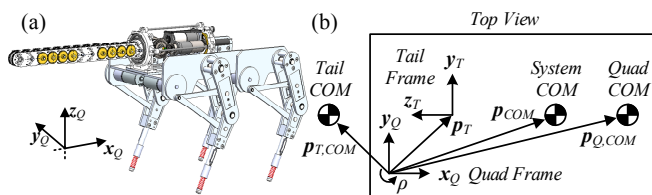


Fig. 16. (a) Integrated quad and tail concept design, and (b) Quad with tail model kinematic variables.

on the rotation of the quadruped is considered. Figure 17 shows the loading profiles for a tail motion at fixed roll  $\varphi = 90^\circ$  with  $\psi_k$  varying from  $-90^\circ$  to  $90^\circ$  in 0.5 sec using the sixth-order polynomial trajectory interpolation in Eqs. 17 and 18. This loading was applied to a Simulink model implementing the z-component of Eq. 22, and a net rotation of  $12.77^\circ$  was calculated based on the  $\dot{\rho}$  trajectory generated by the tail loading and shown in Fig. 18.

Figure 18 also shows the contributions to  $\dot{\rho}$  due to the x-component of  $\mathbf{M}_B$  and the y- and z-components of  $\mathbf{F}_B$  (the other 3 loading components did not contribute). The  $\mathbf{M}_B$  x-component contributes the most to the loading and subsequent rotation ( $10.71^\circ$ , 83.9%), followed by the  $\mathbf{F}_B$  y-component ( $1.80^\circ$ , 14.1%), then the  $\mathbf{F}_B$  z-component ( $0.26^\circ$ , 2%). This is due primarily to the relatively small position vector  $\mathbf{p}_{C2T}$ , compared to the position of the tail COM relative to the tail base frame. Hence,  $\mathbf{M}_B$  significantly overshadows the  $\mathbf{F}_B$  contributions to  $\dot{\rho}$ .

Since this analysis neglects friction at the feet, the time span over which the tail motion occurs is irrelevant. As discussed in [8], static friction at the feet requires high-magnitude moments to initiate motion. Increasing these peak moments can come from increasing the tail mass and reducing the time period of a tail motion, but also from the use of an articulated structure, as demonstrated in this section.

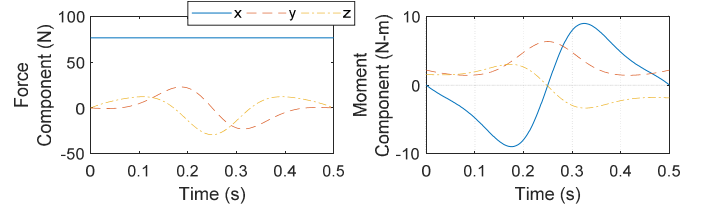


Fig. 17. Tail loading  $\mathbf{F}_B$  and  $\mathbf{M}_B$  applied to quadruped by tail.

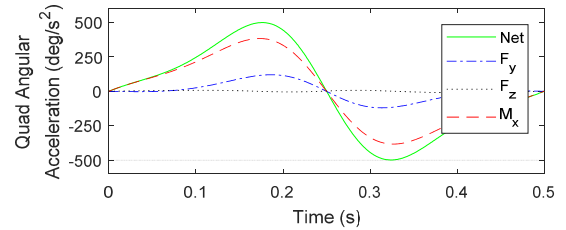


Fig. 18. Net quad yaw acceleration profile and  $F_{B,y}$ ,  $F_{B,z}$ ,  $M_{B,x}$  contributions.

## IX. CONCLUSION AND FUTURE WORK

A novel robotic tail design is presented in this paper that is envisioned for use onboard mobile legged robots to serve as an external source of inertial loading separate from the legs for enhanced performance.

Future work will include the redesign and miniaturization of the tail linkages for metal fabrication and investigating methods of routing high strength cables with minimal friction to prevent structural failures and increase inertial loading profile magnitudes. The articulated tail structure will be modified to incorporate a robotic gripper as an end effector to better grasp and wrap around objects and investigate the enhanced manipulation capabilities provided to a mobile legged robot. Further analysis and dynamic models will be

developed to analytically determine the spatial effects of various spatial tail motions on a variety of legged robots (bipedal and quadrupedal). Furthermore, prescribed torque inner-loop control laws will be designed to replace the prescribed position controller used in these analyses. Outer-loop control laws will also be derived for stabilization, maneuvering and dynamic self-righting. The experimental setup will be further developed to enable hardware-in-the-loop simulations of a virtual legged robot modeled using a multi-body dynamics physics simulator that utilizes real-time measurements of loading profiles generated by the integrated prototype of the R3-RT to conduct various case studies and validate dynamic models and control laws.

## REFERENCES

- [1] W. Rone and P. Ben-Tzvi, "Dynamic Modeling and Simulation of a Yaw-Angle Quadruped Maneuvering With a Planar Robotic Tail," *Journal of Dynamic Systems, Measurement, and Control*, vol. 138, p. 084502, 2016.
- [2] W. Saab and P. Ben-Tzvi, "Design and Analysis of a Discrete Modular Serpentine Tail " in *International Design Engineering Technical Conferences and Computers and Information in Engineering Conference* Charlotte, NC, USA, 2016.
- [3] S.-H. Lee and A. Goswami, "Reaction Mass Pendulum (RMP): An Explicit Model for Centroidal Angular Momentum of Humanoid Robots," in *IEEE International Conference on Robotics and Automation*, 2007, pp. 4667-4672.
- [4] K. Machairas and E. Papadopoulos, "On Quadruped Attitude Dynamics and Control Using Reaction Wheels and Tails," in *European Control Conference*, 2015, pp. 753-758.
- [5] T. Libby, A. M. Johnson, E. Chang-Siu, R. J. Full, and D. E. Koditschek, "Comparative Design, Scaling, and Control of Appendages for Inertial Reorientation," *IEEE Transactions on Robotics*, vol. 32, pp. 1380-1398, 2016.
- [6] A. Patel and E. Boje, "On the Conical Motion of a Two-Degree-of-Freedom Tail Inspired by the Cheetah," *IEEE Transactions on Robotics*, vol. 31, pp. 1555-1560, 2015.
- [7] A. Patel and M. Braae, "Rapid Acceleration and Braking: Inspirations from the Cheetah's Tail," in *IEEE International Conference on Robotics and Automation* 2014, pp. 793-799.
- [8] A. Patel and M. Braae, "Rapid Turning at High-Speed: Inspirations from the Cheetah's Tail," in *IEEE/RSJ International Conference on Intelligent Robots and Systems*, 2013, pp. 5506-5511.
- [9] G.-H. Liu, H.-Y. Lin, H.-Y. Lin, S.-T. Chen, and P.-C. Lin, "A bio-inspired hopping kangaroo robot with an active tail," *Journal of Bionic Engineering*, vol. 11, pp. 541-555, 2014.
- [10] V. Kopman, J. Laut, F. Acquaviva, A. Rizzo, and M. Porfiri, "Dynamic modeling of a robotic fish propelled by a compliant tail," *IEEE Journal of Oceanic Engineering*, vol. 40, pp. 209-221, 2015.
- [11] E. Chang-Siu, T. Libby, M. Tomizuka, and R. J. Full, "A Lizard-Inspired Active Tail Enables Rapid Maneuvers and Dynamic Stabilization in a Terrestrial Robot," in *IEEE/RSJ International Conference on Intelligent Robots and Systems*, 2011, pp. 1887-1894.
- [12] G. He and Z. Geng, "Exponentially stabilizing an one-legged hopping robot with non-SLIP model in flight phase," *Mechatronics*, vol. 19, pp. 364-374, 2009.
- [13] N. Kohut, D. Haldane, D. Zarrouk, and R. Fearing, "Effect of Inertial Tail on Yaw Rate of 45 Gram Legged Robot," in *International Conference on Climbing and Walking Robots and the Support Technologies for Mobile Machines*, 2012, pp. 157-164.
- [14] W. R. Provancher, S. I. Jensen-Segal, and M. A. Fehlbeg, "ROCR: An energy-efficient dynamic wall-climbing robot," *IEEE/ASME Transactions on Mechatronics*, vol. 16, pp. 897-906, 2011.
- [15] F. J. Berenguer and F. M. Monasterio-Huelin, "Zappa, a quasi-passive biped walking robot with a tail: Modeling, behavior, and kinematic estimation using accelerometers," *IEEE Transactions on Industrial Electronics*, vol. 55, pp. 3281-3289, 2008.
- [16] A. Mutka, M. Orsag, and Z. Kovacic, "Stabilizing a Quadruped Robot Locomotion using a Two Degree of Freedom Tail," in *21st Mediterranean Conference on Control & Automation*, 2013, pp. 1336-1342.
- [17] E. Chang-Siu, T. Libby, M. Brown, R. J. Full, and M. Tomizuka, "A Nonlinear Feedback Controller for Aerial Self-Righting by a Tailed Robot," in *International Conference on Robotics and Automation* 2013, pp. 32-39.
- [18] A. De and D. E. Koditschek, "The Penn Jerboa: A platform for exploring parallel composition of templates," *arXiv preprint arXiv:1502.05347*, 2015.
- [19] R. Briggs, J. Lee, M. Haberland, and S. Kim, "Tails in Biomimetic Design: Analysis, Simulation, and Experiment," in *IEEE/RSJ International Conference on Intelligent Robots and Systems* Vilamoura-Algarve, Portugal, 2012, pp. 1473-1480.
- [20] W. S. Rone and P. Ben-Tzvi, "Continuum Robotic Tail Loading Analysis for Mobile Robot Stabilization and Maneuvering," in *International Design Engineering Technical Conferences and Computers and Information in Engineering Conference*, Buffalo, NY, USA, 2014, pp. V05AT08A009-V05AT08A009.
- [21] P. K. Singh and C. M. Krishna, "Continuum arm robotic manipulator: A review," *Universal Journal of Mechanical Engineering*, vol. 2, pp. 193-198, 2014.
- [22] S. Kim, C. Laschi, and B. Trimmer, "Soft robotics: a bioinspired evolution in robotics," *Trends in biotechnology*, vol. 31, pp. 287-294, 2013.
- [23] Z. Li, R. Du, H. Yu, and H. Ren, "Statics Modeling of an Underactuated Wire-Driven Flexible Robotic Arm," in *5th IEEE RAS/EMBS International Conference on Biomedical Robotics and Biomechanics*, 2014, pp. 326-331.
- [24] J.-w. Suh, K.-y. Kim, J.-w. Jeong, and J.-j. Lee, "Design considerations for a hyper-redundant pulleyless rolling joint with elastic fixtures," *IEEE/ASME Transactions on Mechatronics*, vol. 20, pp. 2841-2852, 2015.
- [25] L.-R. Lin and H.-P. Huang, "NTU hand: A new design of dexterous hands," *Journal of Mechanical Design*, vol. 120, pp. 282-292, 1998.
- [26] T. Okada, "Object-handling system for manual industry," *IEEE Transactions on Systems, Man, and Cybernetics*, vol. 9, pp. 79-89, 1979.
- [27] P. J. Kyberd, C. Light, P. H. Chappell, J. M. Nightingale, D. Whatley, and M. Evans, "The design of anthropomorphic prosthetic hands: A study of the Southampton Hand," *Robotica*, vol. 19, pp. 593-600, 2001.
- [28] S. Hirose and Y. Umetani, "The development of soft gripper for the versatile robot hand," *Mechanism and Machine Theory*, vol. 13, pp. 351-359, 1978.
- [29] M. G. Catalano, G. Grioli, E. Farnioli, A. Serio, C. Piazza, and A. Bicchi, "Adaptive synergies for the design and control of the Pisa/IIT SoftHand," *The International Journal of Robotics Research*, vol. 33, pp. 768-782, 2014.
- [30] G. Palli, "Model and control of tendon actuated robots," 2007.
- [31] V. Kamidi, W. Saab, and P. Ben-Tzvi, "Design and Analysis of a Novel Planar Robotic Leg for High-Speed Locomotion," in *IEEE/RSJ International Conference on Intelligent Robots and Systems*, Vancouver, Canada, 2017.